Eocene tearing and fragmentation of Indian lithosphere beneath the Woka rift, southern Tibet

Lin Gong[1], Qiang Wang[1,2*], Andrew C. Kerr[3], Huayong Chen[4], Jingjing Fan[1], Zilong Wang[1], Dongjing Xu[1], Qiji Yang[1]

1 State Key Laboratory of Isotope Geochemistry, Guangzhou Institute of Geochemistry, Chinese Academy of Sciences, Guangzhou 510640, China

2 College of Earth and Planetary Sciences, University of Chinese Academy of Sciences, Beijing 100049, China

3 School of Earth and Environmental Sciences, Cardiff University, Cardiff CF10 3AT, UK

4 Key Laboratory of Mineralogy and Metallogeny, Guangzhou Institute of Geochemistry, Chinese Academy of Sciences, Guangzhou 510640, China

*Corresponding author: Qiang Wang (wqiang@gig.ac.cn)

Guangzhou Institute of Geochemistry (GIG), Chinese Academy of Sciences (CAS), Wushan Street, Guangzhou, 510640, Tel: +86-157-2406-3366, Fax: 86-20-8529-0130

ABSTRACT

When and how the syncontractional north-south trending rifts formed in the Tibetan-Himalayan Plateau are crucial, yet unsolved issues that could help establish the interplay between geodynamic evolution and uplift of the plateau. Recent geophysical observations indicate that although Indian lithosphere tearing is the most likely trigger for rift formation, the timing of this tearing remains uncertain. To address this issue, we studied the Woka rift, which represents a typical north-south trending rift in south Tibet. Our results show that granitoids from the hanging wall and footwall of the Woka rift have significantly different magma crystallization temperatures (770–860 °C vs. 650–750 °C) and crustal thickness (~40 km vs. ~60 km) during the Eocene. These differences were most likely linked to tearing of the Indian lithosphere. The integration of crustal thickness trends and bedrock emplacement depth from the Eocene to the Oligocene suggest that the hanging wall exhumed at a faster rate than the footwall. From this information, it is clear that the Woka rift did not undergo E-W extension during this period. Integrating data from geophysics, thermochronology, mantle-derived, N-S trending dikes and adakitic rocks, we propose that Indian lithospheric tearing and fragmentation during the Eocene caused weakening of the Tibetan middle-lower crust rather than directly triggering surface extension of the Woka rift. This study has significant implications for the deep lithospheric processes and surface responses in the Himalayan-Tibetan Plateau.

Key words Himalayan-Tibetan Plateau, Indian lithosphere, N-S rifts, Deformation, Tearing

IINTRODUCTION

The north-south trending rifts within the Himalayan-Tibetan orogen are crucial in understanding the uplift and geodynamic evolution of the Tibetan Plateau (Molnar and Tapponnier, 1978; Yin, 2000). However, there is still significant disagreement as to when and how these extensional structures formed (Bian et al., 2020b). Many models have been proposed to explain the E-W extension, such as gravitational collapse (Molnar and Tapponnier, 1978), convectional removal of thickened lithosphere (England and Houseman, 1989), eastward extrusion (Armijo et al., 1986), middle-lower crustal flow (Dong et al., 2020), underthrusting of the Indian plate (Styron et al., 2015; Bian et al., 2022), lateral or vertical tearing of the Indian plate (Chen et al., 2015; Webb et al., 2017; Bian et al., 2020b), and back-arc spreading along Eastern Asia margin (Yin, 2000). Recent geophysical observations indicate a broad coupling between the surface rifts and weak mid-lower crustal bands in southern Tibet, suggesting that this coupling is most likely resulted from tearing of the Indian slab (Fig. 1a; Li and Song, 2018; Shi et al., 2020; Hou et al., 2023; Tan et al., 2023). Nevertheless, geophysical data cannot determine when this tearing occurred. Thus, it is essential to establish the temporal and genetic link between the deep lithospheric processes and shallow deformation of the rifts.

Temporal and spatial variations in crustal thickness and magma crystallization

63 conditions are important proxies of deep geodynamic processes (Chapman et al., 2015;
64 Pan et al., 2024), including the transition of tectonic stress, subduction zone migration,
65 lithospheric removal, and asthenosphere upwelling. The obvious impact of the tearing
66 and fragmentation of the subducted Indian continental slab was the heat influx to the
67 overriding plate due to asthenosphere upwelling (Wang et al., 2022; Pan et al., 2024).
68 This would decrease melting depth and increase magma temperature (Pan et al., 2024).
69 Besides, the Indian slab tearing may also give rise to potassic-ultrapotassic rocks, dike
70 intrusions and even porphyry copper deposits in the overriding plate (Wang et al.,
71 2022; Hou et al., 2023; Jarquín et al., 2023). Comparing the differential exhumation
72 between the footwall and hanging wall of the rift is a critical method for constraining
73 the rift displacement, as exemplified in the Cona rift (Bian et al., 2020b). Recently, a
74 study has shown that bedrock pressure patterns of the Gangdese batholith in southern
75 Tibet can provide insights into shallow exhumation or burial processes of crustal
76 rocks (Cao et al., 2020). Consequently, simultaneous variations in crustal thickness,
77 magma crystallization conditions, and bedrock pressure can help determine the
78 interaction between deep dynamic processes and surface responses.

79 In this study, we focused on the Woka rift, the easternmost north-south trending
80 rift in southern Tibet (Fig. 1a). This rift was chosen for two reasons. Firstly,
81 geophysical observations have identified slab tearing beneath the Woka rift (Li and
82 Song, 2018). Secondly, Cenozoic granitic intrusions occurred in both the footwall and
83 hanging wall of the rift. Therefore, lateral variations in shallow exhumation and
84 magma crystallization conditions can be used to infer deep dynamic processes and

their surface responses. Temporal variation of crustal thickness and magma crystallization temperature were constrained by zircon U–Pb dating along with trace element analysis of granitic intrusive rocks from the footwall and hanging wall of the Woka rift. Bedrock pressures were obtained using Al-in-hornblende barometry. The spatial-temporal variation of these parameters, together with compiled N-S trending dikes, potassic-ultrapotassic rocks and adakitic rocks, leads us to propose a refined model for the formation of the Woka rift, in which tearing and fragmentation of the Indian slab initiated in the Eocene but did not directly trigger surface E-W extension.

GEOLOGICAL BACKGROUND AND SAMPLES

Widespread syncontractional extension structures shown by broadly north-south trending rifts or grabens, are prominent characteristics of the Himalayan-Tibetan plateau (Fig. 1a). These active rifts are typically bounded by normal faults and are more extensively developed in the southern part of the plateau (Sundell et al., 2013). From west to east, there are eight rifts, some of which are generally linked to the V-shaped conjugate strike-slip faults along the Bangong-Nujiang suture zone in central Tibet, including the Yadong-Gulu, Pum Qu-Xianza, Tangra Yum Co, and Lunggar rifts (Fig. 1a; Sundell et al., 2013; Bian et al., 2022). The timing of the initial E-W extension across the Himalayan-Tibetan plateau is still debated, with proposed ages spanning from the Eocene to Pliocene (Fig. 1a; Wang et al., 2010; Bian et al., 2020b).

The Woka rift, located in the northern part of the north-south trending

Woka-Cona rift zone, is a half graben that is bounded by the west-dipping Woka normal fault (Fig. 2). It is developed within the Lhasa terrane with a length of ~50 km and terminates at the Indus-Yarlung suture zone. The footwall and hanging wall of the Woka fault both consist of Gangdese batholith rocks from the Cretaceous to Oligocene (Ji et al., 2012; Cao et al., 2020; Shen et al., 2022). Based on thermochronometric data, the normal faulting of the Woka rift appears to have occurred between 12−10 Ma and 5−2 Ma (Dai et al., 2021; Shen et al., 2022; Cai et al., 2023). However, the ca. 18 Ma carbonatitic dikes in the Cona rift and N-S trending lamprophyre dikes to the north of Woka rift suggest an earlier E-W extension (Zhao et al., 2014; Hu et al., 2022). Besides, a much earlier initiation of E-W extension has been identified based on the ca. 43 Ma hydrothermal ore vein that filled the N-S trending normal fault near the Cona rift (Zhou et al., 2018b).

The samples used in this study are all granitic bedrocks that were collected along two profiles across the footwall and hanging wall of the Woka rift (Fig. 2). This sampling strategy was designed to test whether these rocks had undergone differential exhumation and deep geodynamic processes during emplacement.

RATIONALE

Previous studies conducted on the Sierra Nevada and Gandese batholiths have suggested that magmatism, deformation, and surface erosion in an orogen can be linked using a one-dimensional kinematic model (Lee et al., 2015; Cao et al., 2016, 2020). In such a model, a crustal column is thickened by magmatic underplating,

tectonic shortening or burial, while it is thinned by erosion/exhumation, delamination, or tectonic extension (Lee et al., 2015; Cao et al., 2016). In a simple crustal column (Fig. 3), vertical movement of rocks can be described by the following equation:

$$v_e(t) = \frac{dz}{dt} = \dot{\varepsilon}_z \cdot z(t) - E. \quad (1)$$

where z is depth below the surface (positive downward), t is the time, $v_e(t)$ is the exhumation or burial rate at time t, $\dot{\varepsilon}_z$ is thickening strain rate that related to tectonic and magmatic thickening (assuming as a constant), $z(t)$ is the depth at time t and E is the surface erosion rate (assuming as a constant). If we know the initial depth of the rock ($z(0) = z_0$), then the solution of equation (1) is as follows (Cao et al., 2020):

$$z(t) = \left(z_0 - \frac{E}{\dot{\varepsilon}_z}\right) \cdot e^{\dot{\varepsilon}_z t} + \frac{E}{\dot{\varepsilon}_z}. \quad (2)$$

This equation represents the temporal path of exhumation/burial of a rock with a combination of the $\dot{\varepsilon}_z$ and E. To obtain a unique solution for the $\dot{\varepsilon}_z$ and E, we must simultaneously combine at least two varying paths of rocks with different depths at the same crustal column. This can be achieved if we integrate the temporal variations in crustal thickness and emplacement depth of bedrocks.

To determine temporal variations in crustal thickness in the Woka rift, we used zircon U-Pb dating with trace element analysis, based on recent evidence for a positive correlation between zircon Eu/Eu* values and crustal thickness (Tang et al., 2021). We also analyzed the hornblende compositions of the dated granitoids by electron probe microanalysis (EPMA) to determine their paleo-emplacement depth, calculated by Al-in-hornblende barometry. Magmatic crystallization temperatures calculated by Ti-in-zircon thermometer (Ferry and Watson, 2007) were used to infer

possible deep geodynamic processes.

ANALYTICAL METHODS

The zircon grains from 17 granitoids in the Woka rift were separated using conventional magnetic and heavy liquid techniques. In order to characterize the internal structures and choose suitable grains for in-situ analysis, the mounted and polished zircon crystals were imaged by cathodoluminescence (CL) using a TESCAN MIRA3 field emission scanning electron microscope at the Testing Center, Tuoyan Technology Co., Ltd., Guangzhou, China.

Zircon U, Th, and Pb isotopes, as well as trace element analyses, were measured simultaneously using a laser inductively coupled plasma-mass spectrometer (LA-ICP-MS) system at Wuhan SampleSolution Analytical Co., Ltd. in Wuhan, China. Zircon was sampled using a Geolas HD laser ablation system, which includes a MicroLas optical system and a COMPexPro 102 ArF excimer laser with a wavelength of 193 nm and an energy of 80 mJ. The ion-signal intensities were obtained using the Agilent 7900 quadrupole ICP-MS with helium as the carrier gas and argon as the make-up gas. The aerosol was efficiently transported to the ICP-MS by mixing the make-up gas with the carrier gas via a T-connector. The laser ablation system included a 'wire' signal smoothing equipment (Hu et al., 2015). In this study, laser ablation spots were set to 32 μm in diameter with an ablation frequency of 5 Hz. The analysis involved a background acquisition of approximately 20 seconds, followed by 50 seconds of data acquisition from the sample. External standards for U-Pb dating and

trace element calibration were Zircon 91500 and glass NIST610, respectively. After every six sample analyses, two 91500 zircon standards were used. Quality control during U-Pb dating was ensured by using Zircon standard GJ-1, Plešovice, and Tanz. Raw data reduction was performed using the ICPMSDataCal10.8 software (Liu et al., 2010). Concordia diagrams and weighted mean calculations were performed using Isoplot_ver4.15 (Ludwig, 2003). The weighted mean $^{206}Pb/^{238}U$ ages of zircon standards GJ-1, Plešovice, and Tanz were determined to be 601.3 ± 1.9 Ma (1σ; n = 34; Fig. 4r), 337.5 ± 1.3 Ma (1σ; n = 24; Fig. 4s), and 561.5 ± 2.1 Ma (1σ; n = 23; Fig. 4t), respectively. These ages are consistent with recommended values within 2σ (Jackson et al., 2004; Sláma et al., 2008; Hu et al., 2021).

The quantitative analysis of in-situ major elements of hornblende and plagioclase were completed by using a JEOL JXA-iSP100 electron probe microanalyzer at the Testing Center, Tuoyan Technology Co., Ltd., Guangzhou, China. The analysis of hornblende and plagioclase was conducted with an accelerating voltage of 15 KV, a 20 nA beam current, and a beam size of 3-5 μm. The ZAF correction method of JEOL was used for data correction.

RESULTS AND DISCUSSION

Exhumation of the Woka rift during Eocene to Oligocene

The detailed zircon U-Pb isotope and trace element data, along with the calculated crustal thickness and crystallization temperatures, are provided in Table S1. The major element compositions of hornblende and the calculated emplacement depth

195 are presented in Table S2. Ten granitoids from the hanging wall of the Woka rift
196 yielded two zircon U−Pb age clusters at Eocene (ca. 47−41 Ma) and Oligocene (ca.
197 32−24 Ma), respectively (Fig. 4). Except two Late Cretaceous (ca. 74 and ca. 81 Ma)
198 samples, the remaining 5 samples from the footwall of the Woka rift also emplaced at
199 Eocene (ca. 56−42 Ma) and Oligocene (ca. 32 Ma). Given the India-Aisa collision
200 commenced at ~60 Ma (e.g., Kapp and DeCelles, 2019), the two Cretaceous samples
201 are excluded from later discussion because their formation cannot be linked to the
202 subduction of the Indian lithosphere.

203 The crustal thickness of the hanging wall samples shows an increase from ca. 45
204 km to ca. 65 km since ~50 Ma until 20 Ma (Fig. 5a). The thickness of the footwall,
205 however, remains almost constant or slightly increases from 55 to 60 km between 55
206 and 30 Ma (Fig. 5a). Additionally, it seems that both the footwall and hanging wall
207 samples had a slightly greater crustal thickness of 60−70 km between 60 and 55 Ma
208 (Fig. 5a). These crustal thickness values, although calculated using zircon Eu
209 anomalies, are generally consistent with the published crustal thickness calculated by
210 Sr/Y and La/Yb ratios of intermediate-felsic rocks within 2σ if they are
211 tempo-spatially correlated (Fig. 6; Zhu et al., 2023). For instance, thinner local
212 thicknesses of 40-50 km occurred mainly to the west of Woka rift during 55-45 Ma
213 (Fig. 6b-c; Zhu et al., 2023), which is consistent with our results for the hanging wall
214 samples (Fig. 5a). However, it should be noted that some of the crustal thicknesses
215 calculated using whole-rock compositions during 55-45 Ma may have been
216 underestimated due to intense magma mixing (Zhu et al., 2023). Additional data is

still required to verify the spatial variation of crustal thickness during 60-55 Ma due to low data density. Nevertheless, our limited data indicate that crustal thickening primarily took place near the Indus-Yarlung suture during this period (Fig. 6a).

Combined with previous hornblende data (Wang et al., 2014; Cao et al., 2020), the granitoids in the hanging wall were emplaced at ~ 9−13 km during the Eocene and the depth gradually decreased to ~ 3−8 km in the Oligocene (Fig. 5a). In contrast, the footwall granitoids were emplaced at ~ 7−9 km in the Eocene and ~ 5 km in the Oligocene (Fig. 5a). For simplicity, we use the average depth as the emplacement depth of the intrusions. In this way, the emplacement depth of the hanging wall varied from 11 to 5.5 km between 50 and 25 Ma. Similarly, emplacement depth of the footwall varied from 8 to 5 km between 55 and 30 Ma.

Using the varying paths of crustal thickness and emplacement depth through time, Eq. 2 can provide a unique solution for both exhumation rate (E) and strain rate ($\dot{\varepsilon}_z$). The example code is provided in the Supplementary materials (DR1). The calculated results indicate that the hanging wall and footwall of the Woka rift underwent differential exhumation during the Eocene and Oligocene, with exhumation rates of 0.385 km/Ma and 0.195 km/Ma (Fig. 5a), respectively. Although the calculated exhumation rates were estimated as average during the Eocene to Oligocene, the hanging wall was exhumed twice as fast as the footwall. This suggests that the Woka fault should be activated as a reverse fault during this period if it has a similar geometry to the present fault.

Identification of the Indian lithospheric tearing and fragmentation

Fragmentation or tearing of the underthrusting Indian lithosphere with variable geometry has been clearly revealed by geophysical data (Liang et al., 2016; Tan et al., 2023). Such tearing would trigger upwelling of asthenospheric materials and partial melting of overriding Tibetan lithosphere with shallower melting depth and higher magma temperatures than those without asthenospheric upwelling (Pan et al., 2024). It is noteworthy that prior to about 55 Ma, both the footwall and hanging wall of the Woka rift had comparable thick crust (ca. 60–70 km; Fig. 5a and Fig. 6a) and low Ti-in-zircon crystallization temperatures (ca. 700–750 °C; Fig. 5b). However, the crustal thickness of the hanging wall subsequently thinned to about 40 km (Fig. 5a), and the temperature of magma increased to 770–860 °C after ca. 50 Ma (Fig. 5b). Therefore, such a sudden shift implies an asthenospheric upwelling in the deep lithosphere below the hanging wall of the Woka rift since the Eocene. Whereas the footwall to the east did not be affected by this asthenospheric upwelling.

Two prevailing models have been proposed to interpret the Eocene asthenospheric upwelling, magma flare-up and adakitic magmatism in southern Lhasa: a) rollback and breakoff of the Neo-Tethyan oceanic slab (Chung et al., 2005; Zhu et al., 2015; Ji et al, 2016; Lu et al., 2020); b) delamination of Tibetan lithosphere (Kapp et al., 2019; Qi et al., 2021). Based on the tempo-spatial variation of potassic-ultrapotassic rocks, adakitic rocks, dike intrusions, and crustal thickness in the Lhasa terrane, we propose that tearing and fragmentation of the Indian lithosphere, coupled with Tibetan lithospheric delamination, is the most likely cause for the

asthenospheric upwelling beneath the Woka rift during the Eocene. The evidence supporting our refined model is listed below. Firstly, the breakoff of the Neo-Tethyan oceanic slab would give rise to E-W trending magmatic records in southern Lhasa. The widespread occurrence of Paleocene to early Eocene E-W trending mantle-derived mafic dikes is evidence of this slab breakoff (Yue and Ding, 2006; Huang et al., 2016, 2017). However, a series of Eocene N-S trending mantle- or crustal-derived dikes have also been identified in southern Lhasa (Zhou et al., 2018a; Wang et al., 2019). Although previous studies attributed these dikes to slab breakoff (Zhou et al., 2018a; Wang et al., 2019), vertical slab tearing is a more suitable explanation for the E-W trending extension than the lateral detachment of the Neo-Tethyan slab. Secondly, it is worth noting that in Dazi, the Paleocene E-W trending mafic dikes were cut by an early Eocene N-S trending dike (53.2 Ma; Huang et al., 2016), suggesting slab tearing may have taken place at that time. Thirdly, the subducted front of the Indian lithosphere has reached the Yangbajing area in the early Eocene (53.8 Ma) based on a recently discovered potassic intrusion (Long et al., 2022). Combining with the southward migration of adakitic rocks (Fig. 7b), it is likely that southward tearing of Indian lithosphere has occurred since the Eocene. Fourthly, the lateral variation of crustal thickness during 55-50 Ma across the Woka rift indicates that hanging wall of the rift has thinner crust than the footwall (Fig. 6b). This can be caused by steep subduction of the Indian lithosphere, coupled with Tibetan lithosphere removal (Kapp and DeCelles, 2019; Qi et al., 2021). Under this situation, the subducted Indian slab may be torn due to variable subduction angles.

283 During 50-40 Ma, the Indian lithosphere appears to have been fragmented laterally
284 and migrated westward, as shown by the crustal thickness mapping (Fig. 6c). This is
285 also in agreement with the westward migration of adakitic rocks (Fig. 1b) and
286 explains why asthenospheric upwelling only impacted the hanging wall of the Woka
287 rift.

288 Although the Eocene (ca. 43 Ma) E-W extension has been identified in the Cona
289 rift (Zhou et al., 2018b), it is unclear whether this surface brittle extension linked to
290 deep slab tearing or Neo-Tethyan slab breakoff. The evidence to support the slab
291 breakoff model in the Himalayas is mainly based on the ca. 45 Ma oceanic island
292 basalt (OIB)-type gabbros (Ji et al., 2016). But our recent study suggests that most of
293 the Eocene (ca. 48-35 Ma) magmatism and metamorphism in the Himalaya were
294 related to the Indian lithospheric flexure (Ma et al., 2023). The Woka-Cona rift is
295 unique in that Tibetan mantle-derived helium has extended to Himalayas along this
296 rift based on helium-isotope data from geothermal springs (Klemperer et al., 2022).
297 Conversely, a clear boundary for the $^{3}He/^{4}He$ ratios between a crustal domain in the
298 Himalayas and a mantle domain in Tibet has been identified west of the Woka-Cona
299 rift (Klemperer et al., 2022). Therefore, whether the slab tearing and fragmentation
300 model for the Woka rift can be applied to the other N-S rifts across the
301 Tibetan-Himalayan plateau remains further studies. Nevertheless, the tearing of the
302 Indian lithosphere since ca. 25 Ma across the Lhasa terrane can be robustly supported
303 by the southward migration of potassic-ultrapotassic rocks and adakitic rocks (Fig. 7),
304 which is consistent with previous studies (e.g., Guo and Wilson, 2019; Hou et al.,

2023).

Decoupling of Indian lithospheric tearing and surface E-W extension

The post-collisional mantle-derived potassic to ultra-potassic rocks and N-S trending dikes in the Himalayan-Tibetan orogen have been used as proxies to constrain extensional processes in deep lithosphere and uplift of the Tibetan plateau (Turner et al., 1993; Wang et al., 2010). Recent studies on the Yadong-Gulu and Cona rifts have identified a series of mantle-derived N-S trending dikes that were formed during the Oligocene-Early Miocene. These dikes have been interpreted to be linked to E-W extension and tearing of the Indian lithosphere (Hu et al., 2022; Tian et al., 2023). Besides, the identification of Eocene N-S trending mafic dikes in southern Lhasa terrane implies that an earlier onset of E-W extension, although these dikes were previously ascribed to slab breakoff (Zhou et al., 2018a; Wang et al., 2019). Furthermore, the Eocene E-W extension has also been discovered in the Qiangtang terrane to the north based on N-S trending dikes (Wang et al., 2010). These results are consistent with our new discoveries from the Woka rift, which suggest that the subducted Indian lithosphere beneath the rift has been undergoing extension since the Eocene.

Except the N-S trending dike intrusions, the leucogranites derived from fluid-fluxed melting of metasedimentary rocks in the Himalayas have been used to determine deep E-W extension due to fluid-fluxed melting had higher melting temperatures than fluid-absent melting (Gao et al., 2024). This requires anomalous

heat-influx from asthenospheric upwelling that related to Indian lithospheric tearing. Recent studies on the Himalayan leucogranites along the N-S rifts suggest that E-W extension has initiated since the Oligocene (Fan et al., 2024; Gao et al., 2024), which was likely to be linked to Indian lithospheric tearing beneath the Himalayas.

Thermochronological data can serve as a direct indicator of deformation in the shallow crust. However, unlike the N-S trending dikes and leucogranites, all thermochronological data of the N-S trending rifts across the Himalayan-Tibetan plateau show that these rifts were initially formed in the Middle-Late Miocene to Pliocene (Fig. 1a; Bian et al., 2020b; Shen et al., 2022; Cai et al., 2023). This discrepancy suggests that extension of the Indian plate during the Eocene-Oligocene is not directly related to extension of rifts in the shallow crust of the overriding plate. Besides, the variation of crustal thickness and emplacement depth during the Eocene to Oligocene in the Woka rift demonstrate that extensional normal faulting of the rift in the shallow crust did not occur during Indian lithospheric tearing. In contrast, the hanging wall of the rift underwent more rapid exhumation than its footwall counterpart, a feature which was likely induced by westward fragmentation of Indian plate or crustal thickening in response to magma underplating (Fig. 8a). Even during the Miocene, the migration of potassic-ultrapotassic and adakitic rocks suggests a clear southward rifting of the Indian lithosphere in the Lhasa terrane (Fig. 7), but thermochronological data do not favor a direct link between tearing and rift initiation or acceleration (Bian et al., 2022).

Preferred geodynamic model and its implications

Although numerous geodynamic models have been proposed to interpret the formation of N-S trending across the Tibetan-Himalayan plateau (e.g., Bian et al., 2020b), these models, either direct or indirect, can be broadly divided into the following three categories that involved a) the subducted Indian plate; b) the overriding Tibetan lithosphere; and c) far-field effects from the East Asian margin. The models invoked the Indian lithosphere include northward underthrusting (Styron et al., 2015; Bian et al., 2022), southward tearing (Chen et al., 2015; Li and Song, 2018), lateral fragmentation or detachment (Webb et al., 2017; Bian et al., 2020b), oblique convergence and basal shear (McCaffrey and Nabelek, 1998; Zhang et al., 2023), radial spreading or oroclinal bending of the Himalayan arc (Klootwijk et al., 1985). The models invoked the Tibetan lithosphere include eastward extrusion (Armijo et al., 1986), gravitational collapse and convectional thinning (England and Houseman, 1989), lateral flow or shearing of ductile middle-lower crust (Dong et al., 2020; Nie et al., 2023), or even eastward flow of asthenosphere (Yin and Tayor, 2011). The far-field effect model includes the large-scale Pacific and Sunda slab rollback in the East Asian margin (Yin, 2000; Schellart et al., 2019).

Most of the models mentioned above are interrelated, thus it remains unclear which one of these models is the dominant trigger. Nevertheless, the spatial coupling between the surface rifts and the weakened mid-lower crustal layers or Moho uplifts that have been identified by geophysical studies indicates that the tearing of the Indian plate should have played a role in controlling the formation of these rifts. However,

371 the decoupling of the Indian lithosphere tearing and fragmentation from the brittle
372 E-W extension of the Woka rift suggests that the Indian slab tearing model requires
373 revision. We therefore propose that Indian lithospheric tearing and fragmentation
374 during the Eocene did not lead to the extension of overriding Tibetan lithosphere, but
375 instead caused the mid-lower crust of the overriding plate to be weakened due to
376 asthenospheric upwelling (Fig. 8a). The heat influx from asthenosphere could
377 dramatically reduce the viscosity of the lower crust (Bian et al., 2020a). Following the
378 Eocene slab tearing and fragmentation, underthrusting of the Indian lithosphere
379 beneath the Lhasa terrane probably propagated northward from the late Oligocene to
380 the Miocene in accordance with the northward migration of adakitic rocks and
381 potassic-ultrapotassic rocks (Fig. 7). In such scenarios, the weak layers within the
382 overriding plate would be more susceptible to flow and deformation. Therefore, we
383 propose that the lateral flow or shearing of the weakened crust during the Miocene,
384 coupled with northward underthrusting of Indian lithosphere, caused the shallow
385 extension of the Woka rift (Fig. 8b). Lateral flow and strain may be bidirectional away
386 from the rift, based on the low-velocity anomaly in the middle crust in seismic
387 tomography across the Woka rift (Fig. 5c; Tan et al., 2023).

388 Our refined model reconciles the disputed initial timing of E-W extension
389 obtained from thermochronological data and mantle-derived igneous rocks or N-S
390 trending dikes. The decoupling of the Indian lithospheric tearing and fragmentation
391 from the surface extension of the Woka rift provides an excellent case-study of the
392 interplay between deep lithospheric processes and surface responses, with profound

implications for the geodynamics and uplift of the Tibetan plateau.

CONCLUSIONS

Our work from the Woka rift indicates that tearing of the underthrusting Indian lithosphere initiated in the Eocene, but it did not directly trigger surface extension of the rift. Rather, the brittle E-W extension of the Woka rift was caused by lateral flow or strain of the Tibetan middle-lower crust that had been weakened due to slab tearing and asthenospheric upwelling, coupled with northward underthrusting of the Indian plate.

ACKNOLEDGMENTS

This study was financially supported by the National Natural Science Foundation of China (Nos. 42021002 and 4220030169), the Second Tibetan Plateau Scientific Expedition and Research program (STEP) (Grant No. 2019QZKK0702), and China Postdoctoral Science Foundation (2021M703226). We would like to thank the two anonymous reviewers for their constructive comments and suggestions, which greatly improved this manuscript, and the journal editors for editorial handling. This is contribution No. xx from GIGCAS.

REFERENCES

Armijo, R., Tapponnier, P., Mercier, J. L., and Han, T.-L., 1986, Quaternary extension in southern Tibet: Field observations and tectonic implications: Journal of Geophysical Research: Solid Earth, v. 91, no. B14, p. 13803-13872.

Bian, S., Gong, J., Chen, L., Zuza, A. V., Chen, H., Lin, X., Cheng, X., and Yang, R., 2020a, Diachronous uplift in intra-continental orogeny: 2D thermo-mechanical modeling of the India-Asia collision: Tectonophysics, v. 775, p. 228310.

Bian, S., Gong, J., Zuza, A. V., Yang, R., Chen, L., Ji, J., Yu, X., Tian, Y., Yu, Z., Cheng, X., Lin, X., and Chen, H., 2022, Along-Strike Variation in the Initiation Timing of the North-Trending Rifts in Southern Tibet as Revealed From the Yadong-Gulu Rift: Tectonics, v. 41, no. 7, p. e2021TC007091.

Bian, S., Gong, J., Zuza, A. V., Yang, R., Tian, Y., Ji, J., Chen, H., Xu, Q., Chen, L., Lin, X., Cheng, X., Tu, J., and Yu, X., 2020b, Late Pliocene onset of the Cona rift, eastern Himalaya, confirms eastward propagation of extension in Himalayan-Tibetan orogen: Earth and Planetary Science Letters, v. 544, p. 116383.

Cai, D., Wang, X., Li, G., Jiao, R., Kohn, B., Zhu, W., De Grave, J., and Lu, H., 2023, Fault systems impede incision of the Yarlung river into the Tibetan plateau: Communications Earth & Environment, v. 4, no. 1, p. 200.

Cao, W., and Paterson, S., 2016, A mass balance and isostasy model: Exploring the interplay between magmatism, deformation and surface erosion in continental

arcs using central Sierra Nevada as a case study: Geochemistry, Geophysics, Geosystems, v. 17, no. 6, p. 2194-2212.

Cao, W. R., Yang, J. M., Zuza, A. V., Ji, W. Q., Ma, X. X., Chu, X., and Burgess, Q. R., 2020, Crustal tilting and differential exhumation of Gangdese Batholith in southern Tibet revealed by bedrock pressures: Earth and Planetary Science Letters, v. 543, p. 116347.

Chapman, J. B., Ducea, M. N., DeCelles, P. G., and Profeta, L. J. G., 2015, Tracking changes in crustal thickness during orogenic evolution with Sr/Y: An example from the North American Cordillera: Geology, v. 43, no. 10, p. 919-922.

Chen, Y., Li, W., Yuan, X., Badal, J., and Teng, J., 2015, Tearing of the Indian lithospheric slab beneath southern Tibet revealed by SKS-wave splitting measurements: Earth and Planetary Science Letters, v. 413, p. 13-24.

Chung, S.-L., Chu, M.-F., Zhang, Y., Xie, Y., Lo, C.-H., Lee, T.-Y., Lan, C.-Y., Li, X., Zhang, Q., and Wang, Y., 2005, Tibetan tectonic evolution inferred from spatial and temporal variations in post-collisional magmatism: Earth-Science Reviews, v. 68, no. 3, p. 173-196.

Dai, J.-G., Fox, M., Han, X., Tremblay, M. M., Xu, S.-Y., Shuster, D. L., Liu, B.-R., Zhang, J., and Wang, C.-S., 2021, Two Stages of Accelerated Exhumation in the Middle Reach of the Yarlung River, Southern Tibet Since the Mid-Miocene: Tectonics, v. 40, no. 6, p. e2020TC006618.

Dong, H., Wei, W., Jin, S., Ye, G., Jones, A. G., Zhang, L., Jing, J. e., Xie, C., and Yin, Y., 2020, Shaping the Surface Deformation of Central and South Tibetan Plateau:

455 Insights From Magnetotelluric Array Data: Journal of Geophysical Research:
456 Solid Earth, v. 125, no. 9, p. e2019JB019206.
457 England, P., and Houseman, G., 1989, Extension during continental convergence, with
458 application to the Tibetan Plateau: Journal of Geophysical Research: Solid Earth,
459 v. 94, no. B12, p. 17561-17579.
460 Fan, J., Zhang, X., Ma, L., Wang, Q., Jiang, Z., Xia, X., Wei, G., Wang, Z., Zhou, J.,
461 Li, Q., Liu, X., Huang, T., Zhang, M., and Liu, J., 2024, Formation of
462 Eocene−Miocene felsic magmatic rocks along N-S−trending
463 Yardoi-Kongbugang mountain ranges in the eastern Himalaya: New insights into
464 surface uplift and the initiation of E-W extension in southern Tibet: GSA Bulletin,
465 v. 136, no. 1-2, p. 433-446.
466 Ferry, J. M., and Watson, E. B., 2007, New thermodynamic models and revised
467 calibrations for the Ti-in-zircon and Zr-in-rutile thermometers: Contributions to
468 Mineralogy and Petrology, v. 154, no. 4, p. 429-437.
469 Gao, L.-E., Zeng, L., Zhao, L., Yan, L., Hou, K., and Wang, Q., 2024, Fluid-fluxed
470 melting in the Himalayan orogenic belt: Implications for the initiation of E-W
471 extension in southern Tibet: GSA Bulletin, v. 136, no. 3-4, p. 989-1002.
472 Guo, Z., and Wilson, M., 2019, Late Oligocene–early Miocene transformation of
473 postcollisional magmatism in Tibet: Geology, v. 47, no. 8, p. 776-780.
474 Hou, Z., Wang, R., Zhang, H., Zheng, Y., Jin, S., Thybo, H., Weinberg, R. F., Xu, B.,
475 Yang, Z., Hao, A.-W., Gao, L., and Zhang, L., 2023, Formation of giant copper

476 deposits in Tibet driven by tearing of the subducted Indian plate: Earth-Science
477 Reviews, v. 243, p. 104482.
478 Hu, G., Zeng, L., Gao, L.-E., and Chen, H., 2022, Miocene tearing of Himalayan
479 lithospheric mantle: Evidence from mantle-derived silicocarbonatites from the
480 Cona rift: Chemical Geology, v. 611, p. 121119.
481 Huang, F., Xu, J.-F., Chen, J.-L., Wu, J.-B., Zeng, Y.-C., Xiong, Q.-W., Chen, X.-F.,
482 and Yu, H.-X., 2016, Two Cenozoic tectonic events of N–S and E–W extension
483 in the Lhasa Terrane: Evidence from geology and geochronology: Lithos, v. 245,
484 p. 118-132.
485 Huang, F., Xu, J., Zeng, Y., Chen, J., Wang, B., Yu, H., Chen, L., Huang, W., and Tan,
486 R., 2017, Slab Breakoff of the Neo-Tethys Ocean in the Lhasa Terrane Inferred
487 From Contemporaneous Melting of the Mantle and Crust: Geochemistry,
488 Geophysics, Geosystems, v. 18, no. 11, p. 4074-4095.
489 Jarquín, E., Wang, R., Sun, W.-R., Luo, C.-H., and Xia, W.-J., 2023, Impact of slab
490 tearing along the Yadong-Gulu rift on Miocene alkaline volcanism from the
491 Lhasa terrane to the Himalayas, southern Tibet: GSA Bulletin.
492 Ji, W.-Q., Wu, F.-Y., Liu, C.-Z., and Chung, S.-L., 2012, Early Eocene crustal
493 thickening in southern Tibet: New age and geochemical constraints from the
494 Gangdese batholith: Journal of Asian Earth Sciences, v. 53, p. 82-95.
495 Ji, W., Wu, F., Chung, S., Wang, X., Liu, C., Li, Q., Liu, Z., Liu, X., and Wang, J.,
496 2016, Eocene Neo-Tethyan slab breakoff constrained by 45 Ma oceanic island
497 basalt–type magmatism in southern Tibet: Geology, v. 44, no. 4, p. 283-286.

Kapp, P., and DeCelles, P. G., 2019, Mesozoic–Cenozoic geological evolution of the Himalayan-Tibetan orogen and working tectonic hypotheses: American Journal of Science, v. 319, no. 3, p. 159-254.

Klemperer, S. L., Zhao, P., Whyte, C. J., Darrah, T. H., Crossey, L. J., Karlstrom, K. E., Liu, T., Winn, C., Hilton, D. R., and Ding, L., 2022, Limited underthrusting of India below Tibet: 3He/4He analysis of thermal springs locates the mantle suture in continental collision: Proceedings of the National Academy of Sciences, v. 119, no. 12, p. e2113877119.

Klootwijk, C. T., Conaghan, P. J., and Powell, C. M., 1985, The Himalayan Arc: large-scale continental subduction, oroclinal bending and back-arc spreading: Earth and Planetary Science Letters, v. 75, no. 2, p. 167-183.

Lee, C.-T. A., Thurner, S., Paterson, S., and Cao, W., 2015, The rise and fall of continental arcs: Interplays between magmatism, uplift, weathering, and climate: Earth and Planetary Science Letters, v. 425, p. 105-119.

Li, J., and Song, X., 2018, Tearing of Indian mantle lithosphere from high-resolution seismic images and its implications for lithosphere coupling in southern Tibet: Proceedings of the National Academy of Sciences, v. 115, no. 33, p. 8296.

Liang, X., Chen, Y., Tian, X., Chen, Y. J., Ni, J., Gallegos, A., Klemperer, S. L., Wang, M., Xu, T., Sun, C., Si, S., Lan, H., and Teng, J., 2016, 3D imaging of subducting and fragmenting Indian continental lithosphere beneath southern and central Tibet using body-wave finite-frequency tomography: Earth and Planetary Science Letters, v. 443, p. 162-175.

520 Lu, T.-Y., He, Z.-Y., and Klemd, R., 2020, Two phases of post-onset collision adakitic
521 magmatism in the southern Lhasa subterrane, Tibet, and their tectonic
522 implications: GSA Bulletin, v. 132, no. 7-8, p. 1587-1602.
523 Ma, L., Wang, Q., Kerr, A. C., Li, Z.-X., Dan, W., Yang, Y.-N., Zhou, J.-S., Wang, J.,
524 and Li, C., 2023, Eocene magmatism in the Himalaya: Response to lithospheric
525 flexure during early Indian collision?: Geology, v. 51, no. 1, p. 96-100.
526 McCaffrey, R., and Nabelek, J., 1998, Role of oblique convergence in the active
527 deformation of the Himalayas and southern Tibet plateau: Geology, v. 26, no. 8,
528 p. 691-694.
529 Molnar, P., and Tapponnier, P., 1978, Active tectonics of Tibet: Journal of Geophysical
530 Research: Solid Earth, v. 83, no. B11, p. 5361-5375.
531 Nie, S., Tian, X., Liang, X., and Wan, B., 2023, Less-Well-Developed Crustal
532 Channel-Flow in the Central Tibetan Plateau Revealed by Receiver Function and
533 Surface Wave Joint Inversion: Journal of Geophysical Research: Solid Earth, v.
534 128, no. 4, p. e2022JB025747.
535 Pan, F., Zhang, H., He, X., Harris, N., Dai, H.-K., Xiong, Q., Luo, B., Liu, D., Kusky,
536 T., and Sadiq, I., 2024, Lithosphere tearing and foundering during continental
537 subduction: Insights from Oligocene−Miocene magmatism in southern Tibet:
538 GSA Bulletin, v. 136, no. 1-2, p. 583-596.
539 Qi, Y., Hawkesworth, C. J., Wang, Q., Wyman, D. A., Li, Z.-X., Dong, H., Ma, T.,
540 Chen, F., Hu, W.-L., and Zhang, X.-Z., 2021, Syn-collisional magmatic record of
541 Indian steep subduction by 50 Ma: GSA Bulletin, v. 133, no. 5-6, p. 949-962.

542 Schellart, W. P., Chen, Z., Strak, V., Duarte, J. C., and Rosas, F. M., 2019, Pacific
543 subduction control on Asian continental deformation including Tibetan extension
544 and eastward extrusion tectonics: Nature Communications, v. 10, no. 1, p. 4480.
545 Shen, T., Wang, G., van der Beek, P., Bernet, M., Chen, Y., Zhang, P., Wang, A., and
546 Cao, K., 2022, Impacts of late Miocene normal faulting on Yarlung Tsangpo
547 River evolution, southeastern Tibet: GSA Bulletin, v. 134, no. 11-12, p.
548 3142-3154.
549 Shi, D., Klemperer, S. L., Shi, J., Wu, Z., and Zhao, W., 2020, Localized foundering
550 of Indian lower crust in the India–Tibet collision zone: Proceedings of the
551 National Academy of Sciences, v. 117, no. 40, p. 24742-24747.
552 Styron, R., Taylor, M., and Sundell, K., 2015, Accelerated extension of Tibet linked to
553 the northward underthrusting of Indian crust: Nature Geoscience, v. 8, no. 2, p.
554 131-134.
555 Sundell, K. E., Taylor, M. H., Styron, R. H., Stockli, D. F., Kapp, P., Hager, C., Liu, D.
556 L., and Ding, L., 2013, Evidence for constriction and Pliocene acceleration of
557 east-west extension in the North Lunggar rift region of west central Tibet:
558 Tectonics, v. 32, no. 5, p. 1454-1479.
559 Tan, P., Liang, X., Li, W., and Wu, C., 2023, Crustal structure of the Tibetan Plateau
560 and adjacent areas revealed from ambient noise tomography: Gondwana
561 Research, v. 121, p. 1-15.

562 Tang, M., Ji, W.-Q., Chu, X., Wu, A., and Chen, C., 2021, Reconstructing crustal
563 thickness evolution from europium anomalies in detrital zircons: Geology, v. 49,
564 no. 1, p. 76-80.
565 Tian, Y., Zeng, L., Shen, Y., Yan, L., Zhao, L., Xu, Q., Li, G., and Di, Y., 2023,
566 Melting a melt-metasomatized subcontinental lithospheric mantle: Evidence
567 from Oligocene lamproites within the Gangdese batholith, southern Tibet: Lithos,
568 v. 448-449, p. 107163.
569 Turner, S., Hawkesworth, C., Liu, J., Rogers, N., Kelley, S., and van Calsteren, P.,
570 1993, Timing of Tibetan uplift constrained by analysis of volcanic rocks: Nature,
571 v. 364, no. 6432, p. 50-54.
572 Wang, Q., Wyman, D. A., Li, Z.-X., Sun, W., Chung, S.-L., Vasconcelos, P. M., Zhang,
573 Q., Dong, H., Yu, Y., Pearson, N., Qiu, H., Zhu, T., and Feng, X., 2010, Eocene
574 north–south trending dikes in central Tibet: New constraints on the timing of
575 east–west extension with implications for early plateau uplift?: Earth and
576 Planetary Science Letters, v. 298, no. 1, p. 205-216.
577 Wang, R., Richards, J. P., Hou, Z.-q., Yang, Z.-m., Gou, Z.-b., and DuFrane, S. A.,
578 2014, Increasing Magmatic Oxidation State from Paleocene to Miocene in the
579 Eastern Gangdese Belt, Tibet: Implication for Collision-Related Porphyry
580 Cu-Mo ± Au Mineralization: Economic Geology, v. 109, no. 7, p. 1943-1965.
581 Wang, R., Weinberg, R. F., Zhu, D.-C., Hou, Z.-Q., and Yang, Z.-M., 2022, The
582 impact of a tear in the subducted Indian plate on the Miocene geology of the
583 Himalayan-Tibetan orogen: GSA Bulletin, v. 134, no. 3-4, p. 681-690.

584 Wang, X., Lang, X., Deng, Y., Xie, F., Lou, Y., Zhang, H., and Yang, Z., 2019, Eocene
585 diabase dikes in the Tangbai area, southern margin of Lhasa terrane, Tibet:
586 Evidence for the slab break-off of the Neo-Tethys Ocean: Geology in China, v.
587 46, no. 6, p. 1336-1355.
588 Webb, A. A. G., Guo, H., Clift, P. D., Husson, L., Müller, T., Costantino, D., Yin, A.,
589 Xu, Z., Cao, H., and Wang, Q., 2017, The Himalaya in 3D: Slab dynamics
590 controlled mountain building and monsoon intensification: Lithosphere, v. 9, no.
591 4, p. 637-651.
592 Yin, A., 2000, Mode of Cenozoic east-west extension in Tibet suggesting a common
593 origin of rifts in Asia during the Indo-Asian collision: Journal of Geophysical
594 Research: Solid Earth, v. 105, no. B9, p. 21745-21759.
595 Yin, A., and Taylor, M. H., 2011, Mechanics of V-shaped conjugate strike-slip faults
596 and the corresponding continuum mode of continental deformation: GSA
597 Bulletin, v. 123, no. 9-10, p. 1798-1821.
598 Yue, Y., and Ding, L., 2006, $^{40}Ar/^{39}Ar$ Geochronology, geochemical characteristics
599 and genesis of the Linzhou basic dikes, Tibet: Acta Petrologica Sinica, v. 22, no.
600 4, p. 855-866.
601 Zhang, B., Bao, X., Wu, Y., Xu, Y., and Yang, W., 2023, Southern Tibetan rifting since
602 late Miocene enabled by basal shear of the underthrusting Indian lithosphere:
603 Nature Communications, v. 14, no. 1, p. 2565.
604 Zhao, J., Qin, K., Li, G., Li, J., Xiao, B., Chen, L., Yang, Y., Li, C., and Liu, Y., 2014,
605 Collision-related genesis of the Sharang porphyry molybdenum deposit, Tibet:

606 Evidence from zircon U–Pb ages, Re–Os ages and Lu–Hf isotopes: Ore Geology
607 Reviews, v. 56, p. 312-326.
608 Zhou, B., Han, K., Qiao, X., Pan, L., Wang, F., and Zhao, H., 2018a, Paleogene
609 bimodal intrusions dike in Riduo, Tibet: geochemistry, geochronology and
610 implications for extension: Mineral Exploration, v. 9, no. 9, p. 1746-1757.
611 Zhou, Q., Sun, H. S., Evans, N., Li, C., Liu, Z., Zhang, Q. C., Yan, G. Q., and Huang,
612 J. H., 2018b, Contemporaneous east–west extension and north–south
613 compression at 43 Ma in the Himalayan orogen: Journal of Structural Geology, v.
614 117, p. 124-135.
615 Zhu, D.-C., Wang, Q., Weinberg, R. F., Cawood, P. A., Zhao, Z., Hou, Z.-Q., and Mo,
616 X.-X., 2023, Continental Crustal Growth Processes Recorded in the Gangdese
617 Batholith, Southern Tibet: Annual Review of Earth and Planetary Sciences, v. 51,
618 no. 1, p. 155-188.
619 Zhu, D.-C., Wang, Q., Zhao, Z.-D., Chung, S.-L., Cawood, P. A., Niu, Y., Liu, S.-A.,
620 Wu, F.-Y., and Mo, X.-X., 2015, Magmatic record of India-Asia collision:
621 Scientific Reports, v. 5, no. 1, p. 14289.

622 **Figure captions**

623

624 **Figure 1**. (**a**) Geological map, geography, and S-wave seismic velocity variations of
625 the Himalayan-Tibetan Plateau at 30 km depth. (**b**) Longitudinal distribution of the
626 potassic-ultrapotassic and adakitic magmatism in the Lhasa terrane. The S-wave
627 velocity map in panel a is modified after Tan et al. (2023). The N-S trending rifts are
628 modified from Bian et al. (2020b). The timing of the E-W extension, based on N-S
629 trending or mantle-derived dikes (diamond) and thermochronological data (dot), were
630 provided in Table S4. The compiled data for adakitic rocks and potassic-ultrapotassic
631 rocks in the Lhasa terrane are provided in Table S5 and Table S6, respectively.

632

633 **Figure 2**. Topography of the Woka rift and sample distribution.

634

635 **Figure 3**. Schematic model of one-dimensional kinematics to illustrate the vertical
636 motion of crustal rocks (modified after Cao et al., 2020). (**a**) Simultaneous crustal
637 thickening and surface erosion; (**b**) Simultaneous crustal thinning and surface erosion.
638 Assuming that crustal thickening, thinning, and surface erosion are homogeneous
639 through time. Z-axis is the depth of the rocks below the surface (positive downward).
640 Thickening via magma underplating or compressive deformation would cause rocks
641 to move downward (burial). Conversely, thinning via extensional deformation,
642 delamination or surface erosion would cause rocks to move upward (exhumation).
643 Arrows show the direction and magnitude of crustal rocks moving. ΔH is the variation

644 of elevation in response to thickening or thinning of the crust. Neutral depth is the
645 balance depth between thickening-induced burial and erosional exhumation.
646
647 **Figure 4**. U-Pb concordia diagrams and weighted mean ages for zircons from the
648 granitoids in the Woka rift (**a-q**) and the zircon standards (**r-t**). Only the dates in red
649 were considered to calculate the emplacement ages of the granitoids. The blue, green,
650 and black dates in panels a-q were removed due to low concordance or because they
651 represent the ages of the inherited or xenocrystal zircons. The detailed comments for
652 each grain are given in Table S1.
653
654 **Figure 5**. (**a**) Variation patterns of crustal thickness and emplacement depth of
655 bedrocks in the Woka rift. (**b**) Zircon crystallization temperature for the granitoids in
656 the Woka rift. (**c**) S-wave velocity profile A-A' (see Fig. 1a) across the Woka rift
657 (modified after Tan et al., 2023). Based on the calculated crustal thickness and
658 emplacement depth (Table S3), we assumed that the crustal thickness of the footwall
659 was 55 km at 55 Ma and slightly increased to 60 km at 30 Ma. Meanwhile, the
660 emplacement depth was 8 km at 50 Ma and thinned to 5 km at 30 Ma. Similarly, the
661 crustal thickness of the hanging wall was 45 km at 50 Ma and thickened to 65 km at
662 20 Ma. Whereas the emplacement depth was 11 km at 50 Ma and thinned to 5.5 km at
663 25 Ma. These values were used to calculate the exhumation and strain rates for the
664 hanging wall and footwall of the Woka rift using Equation 2, and the calculated
665 results were then used to forward model the exhumation-burial paths (dotted line) of

666 the crustal rocks. It should be noted that these paths are simply equivalent average
667 estimates due to the limited data available during the late Eocene to early Oligocene.
668 Therefore, distinguishing between two-stage and gradual trends can be difficult.
669
670 **Figure 6**. Contours of calculated crustal thickness around the Woka rift. Crustal
671 thickness data calculated from whole-rock geochemical compositions of
672 intermediate-felsic rocks are compiled from Zhu et al. (2023). Sample distributions
673 are represented by diamond symbols, and faults are modified from Shen et al. (2022).
674 GCT = Great Counter Thrust.
675
676 **Figure 7**. Perpendicular variations of Cenozoic potassic-ultrapotassic rocks (**a**) and
677 adakitic rocks (**b**) relative to the Indus-Yarlung suture zone. Detailed data are given in
678 Table S5 and Table S6.
679
680 **Figure 8**. Geodynamic model showing the formation of the Woka rift in the
681 Eocene-Oligocene (**a**) and Miocene to present (**b**).
682

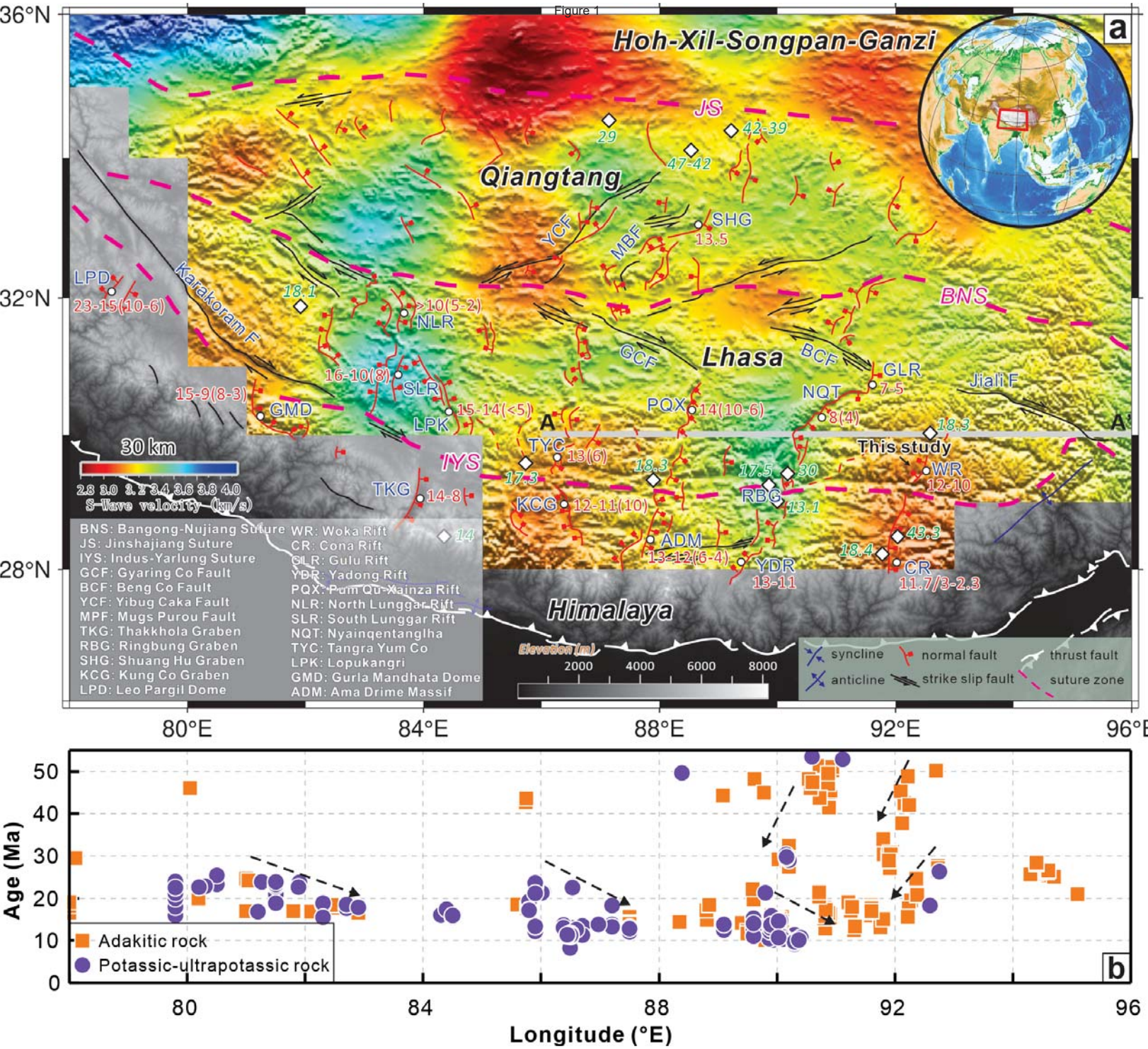
a
Hoh-Xil-Songpan-Ganzi
Qiangtang
Lhasa
Himalaya
JS
BNS
IYS
YCF
MBF
GCF
BCF
Karakoram F
Jiali F
LPD
23-15(10-6)
18.1
>10(5-2)
NLR
16-10(8)
SLR
15-9(8-3)
GMD
15-14(<5)
LPK
29
42-39
47-42
SHG
13.5
PQX
14(10-6)
NQT
8(4)
GLR
7-5
18.3
This study
WR
12-10
TYC
13(6)
17.3
TKG
14-8
14
KCG
12-11(10)
ADM
13-12(6-4)
RBG
17.5
30
13.1
YDR
13-11
43.3
18.4
CR
11.7/3-2.3
A
A'
30 km
2.8 3.0 3.2 3.4 3.6 3.8 4.0
S-wave velocity (km/s)
BNS: Bangong-Nujiang Suture
JS: Jinshajiang Suture
IYS: Indus-Yarlung Suture
GCF: Gyaring Co Fault
BCF: Beng Co Fault
YCF: Yibug Caka Fault
MPF: Mugs Purou Fault
TKG: Thakkhola Graben
RBG: Ringbung Graben
SHG: Shuang Hu Graben
KCG: Kung Co Graben
LPD: Leo Pargil Dome
WR: Woka Rift
CR: Cona Rift
GLR: Gulu Rift
YDR: Yadong Rift
PQX: Pum Qu-Xainza Rift
NLR: North Lunggar Rift
SLR: South Lunggar Rift
NQT: Nyainqentanglha
TYC: Tangra Yum Co
LPK: Lopukangri
GMD: Gurla Mandhata Dome
ADM: Ama Drime Massif
Elevation (m)
2000 4000 6000 8000
syncline
anticline
normal fault
strike slip fault
thrust fault
suture zone
36°N
32°N
28°N
80°E
84°E
88°E
92°E
96°E

Age (Ma)
50
40
30
20
10
0
Adakitic rock
Potassic-ultrapotassic rock
b
80
84
88
92
96
Longitude (°E)

Figure 2

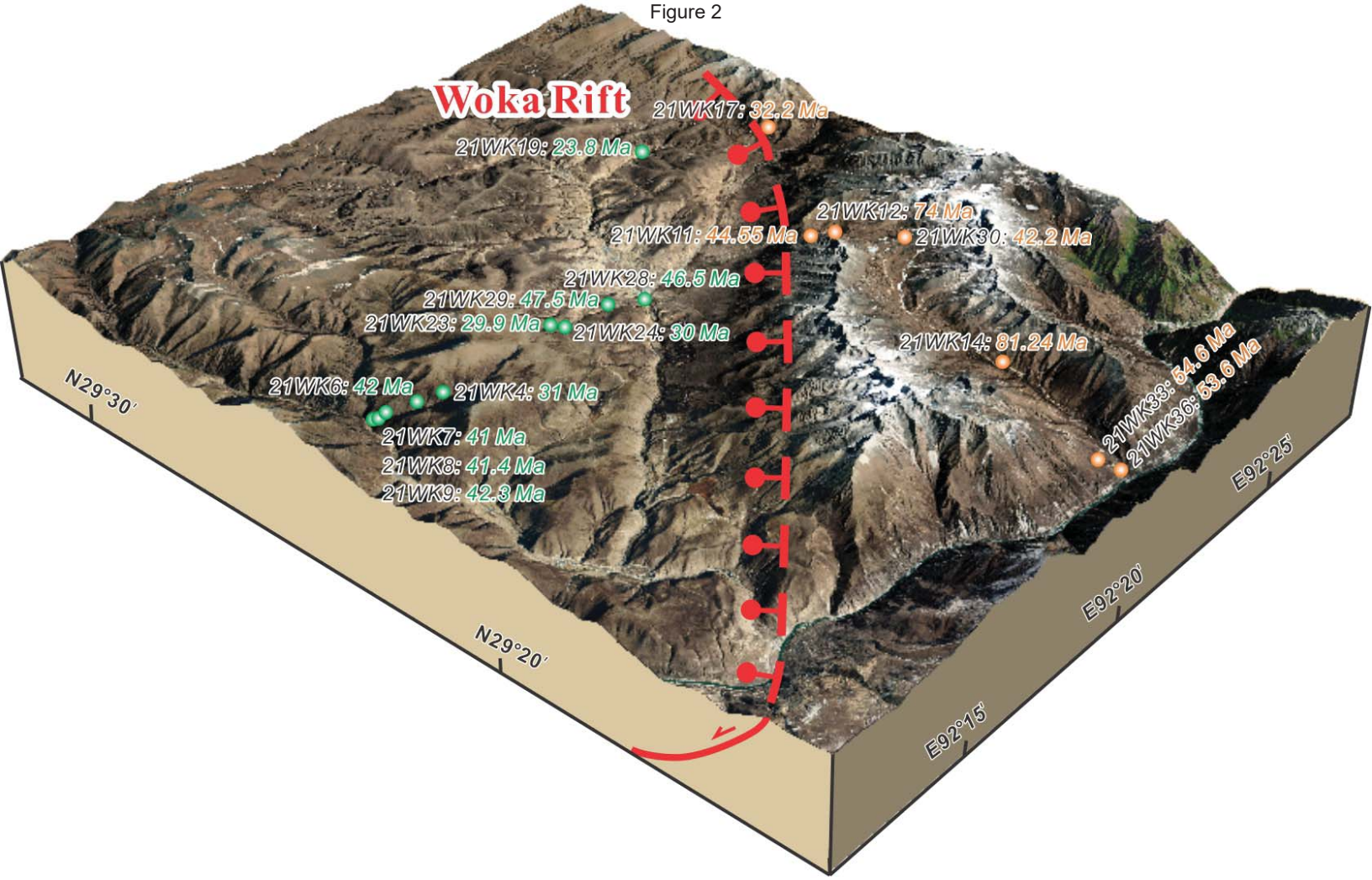
Woka Rift
21WK17: 32.2 Ma
21WK19: 23.8 Ma
21WK12: 74 Ma
21WK11: 44.55 Ma
21WK30: 42.2 Ma
21WK28: 46.5 Ma
21WK29: 47.5 Ma
21WK23: 29.9 Ma
21WK24: 30 Ma
21WK14: 81.24 Ma
21WK6: 42 Ma
21WK4: 31 Ma
21WK7: 41 Ma
21WK8: 41.4 Ma
21WK9: 42.3 Ma
21WK33: 54.6 Ma
21WK36: 53.6 Ma
N29°30′
N29°20′
E92°25′
E92°20′
E92°15′

Figure 3

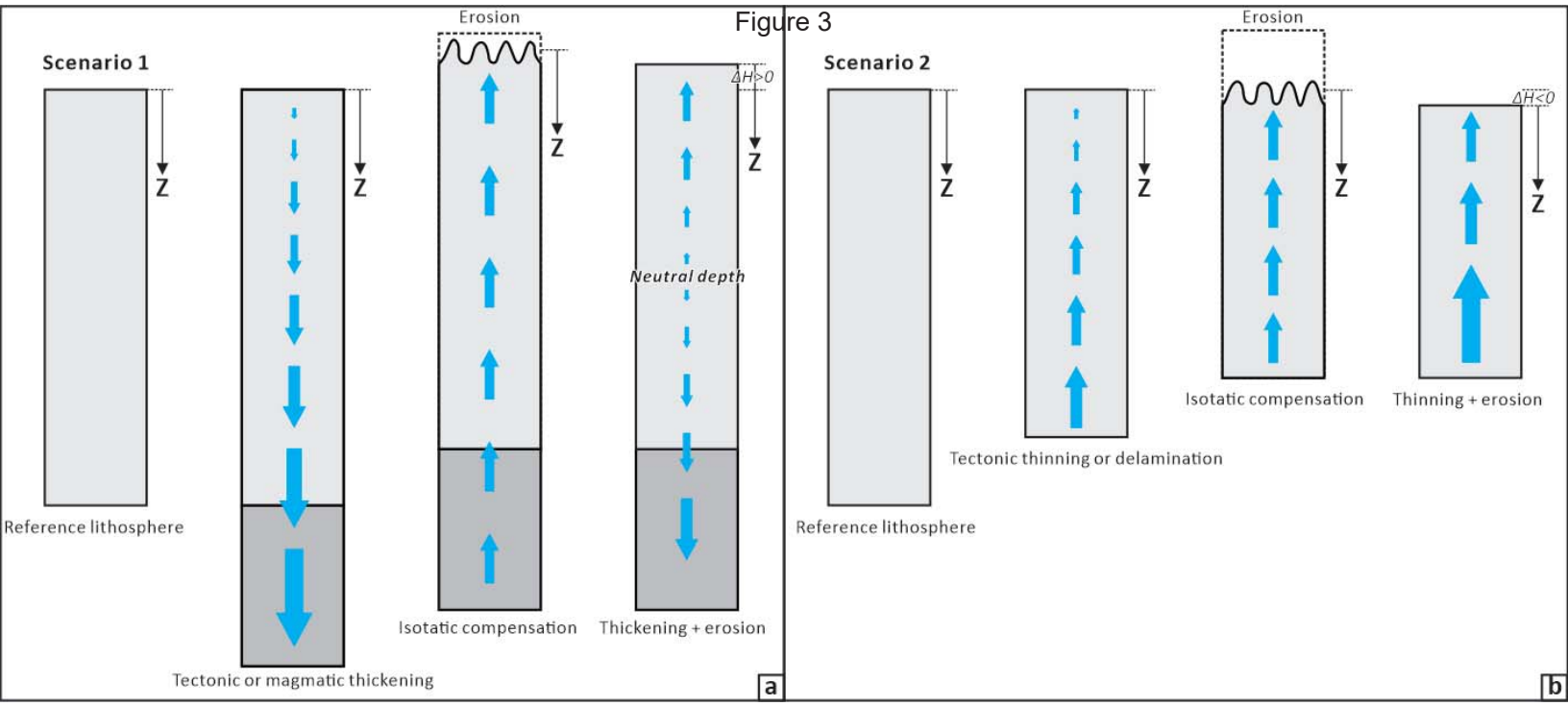
Scenario 1
Z
Reference lithosphere
Tectonic or magmatic thickening
Erosion
Isotatic compensation
ΔH>0
Neutral depth
Thickening + erosion
a
Scenario 2
Tectonic thinning or delamination
Isotatic compensation
ΔH<0
Thinning + erosion
b

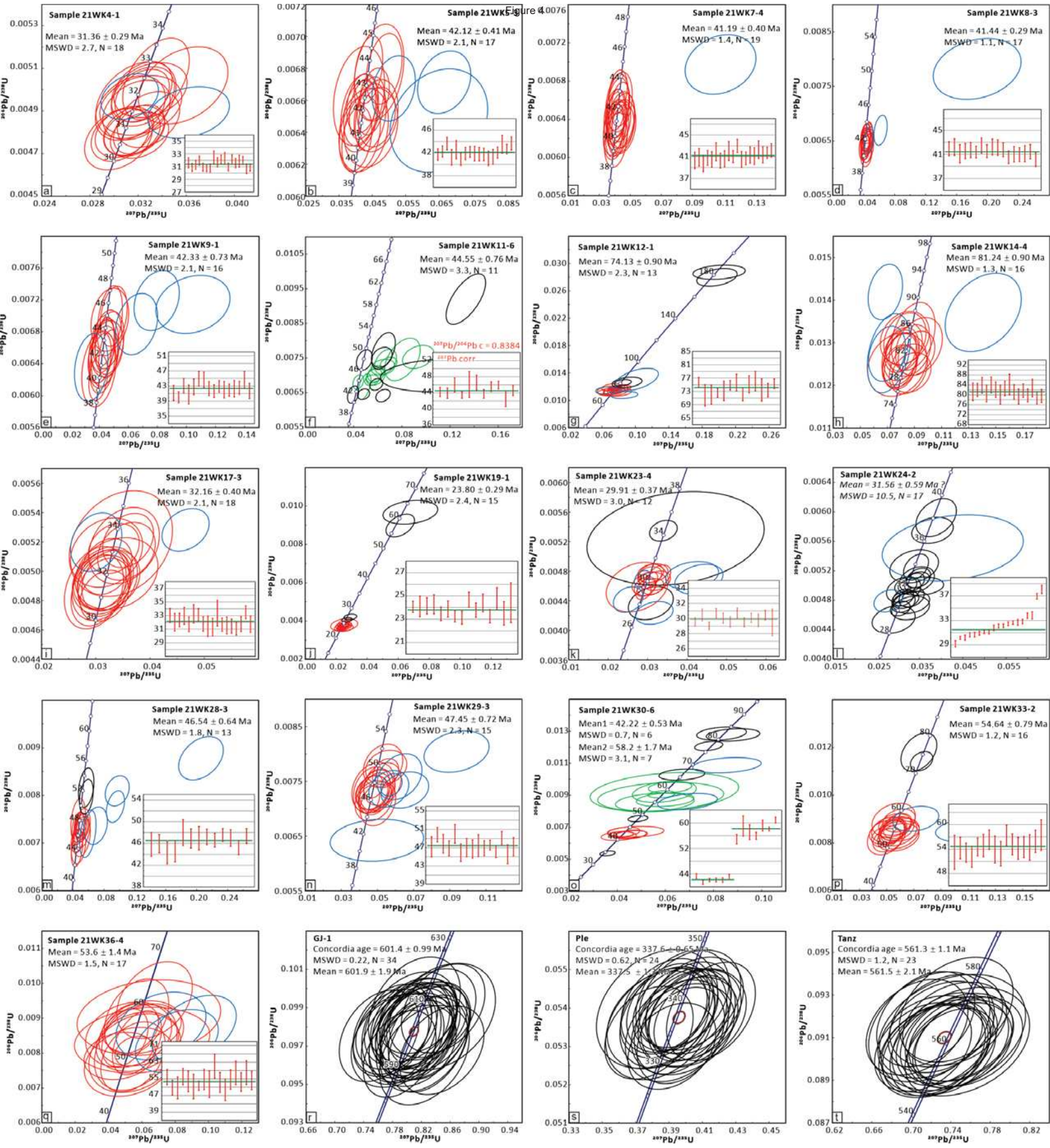
Sample 21WK4-1
Mean = 31.36 ± 0.29 Ma
MSWD = 2.7, N = 18
Sample 21WK5-3
Mean = 42.12 ± 0.41 Ma
MSWD = 2.1, N = 17
Sample 21WK7-4
Mean = 41.19 ± 0.40 Ma
MSWD = 1.4, N = 19
Sample 21WK8-3
Mean = 41.44 ± 0.29 Ma
MSWD = 1.1, N = 17
Sample 21WK9-1
Mean = 42.33 ± 0.73 Ma
MSWD = 2.1, N = 16
Sample 21WK11-6
Mean = 44.55 ± 0.76 Ma
MSWD = 3.3, N = 11
207Pb/204Pb c = 0.8384
207Pb corr
Sample 21WK12-1
Mean = 74.13 ± 0.90 Ma
MSWD = 2.3, N = 13
Sample 21WK14-4
Mean = 81.24 ± 0.90 Ma
MSWD = 1.3, N = 16
Sample 21WK17-3
Mean = 32.16 ± 0.40 Ma
MSWD = 2.1, N = 18
Sample 21WK19-1
Mean = 23.80 ± 0.29 Ma
MSWD = 2.4, N = 15
Sample 21WK23-4
Mean = 29.91 ± 0.37 Ma
MSWD = 3.0, N = 12
Sample 21WK24-2
Mean = 31.56 ± 0.59 Ma ?
MSWD = 10.5, N = 17
Sample 21WK28-3
Mean = 46.54 ± 0.64 Ma
MSWD = 1.8, N = 13
Sample 21WK29-3
Mean = 47.45 ± 0.72 Ma
MSWD = 2.3, N = 15
Sample 21WK30-6
Mean1 = 42.22 ± 0.53 Ma
MSWD = 0.7, N = 6
Mean2 = 58.2 ± 1.7 Ma
MSWD = 3.1, N = 7
Sample 21WK33-2
Mean = 54.64 ± 0.79 Ma
MSWD = 1.2, N = 16
Sample 21WK36-4
Mean = 53.6 ± 1.4 Ma
MSWD = 1.5, N = 17
GJ-1
Concordia age = 601.4 ± 0.99 Ma
MSWD = 0.22, N = 34
Mean = 601.9 ± 1.9 Ma
Ple
Concordia age = 337.6 ± 0.65 Ma
MSWD = 0.62, N = 24
Mean = 337.5 ± 1.3 Ma
Tanz
Concordia age = 561.3 ± 1.1 Ma
MSWD = 1.2, N = 23
Mean = 561.5 ± 2.1 Ma
206Pb/238U
207Pb/235U

Figure 4

Figure 5

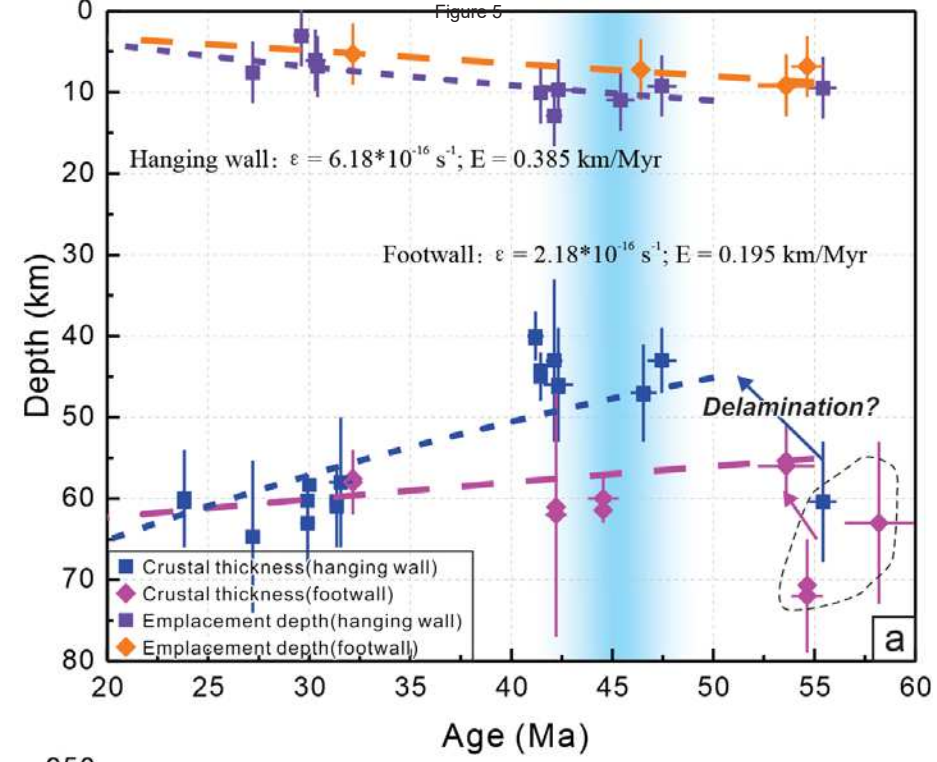
Hanging wall: ε = 6.18*10^-16 s^-1; E = 0.385 km/Myr
Footwall: ε = 2.18*10^-16 s^-1; E = 0.195 km/Myr
Delamination?
Crustal thickness(hanging wall)
Crustal thickness(footwall)
Emplacement depth(hanging wall)
Emplacement depth(footwall)
Depth (km)
Age (Ma)
a

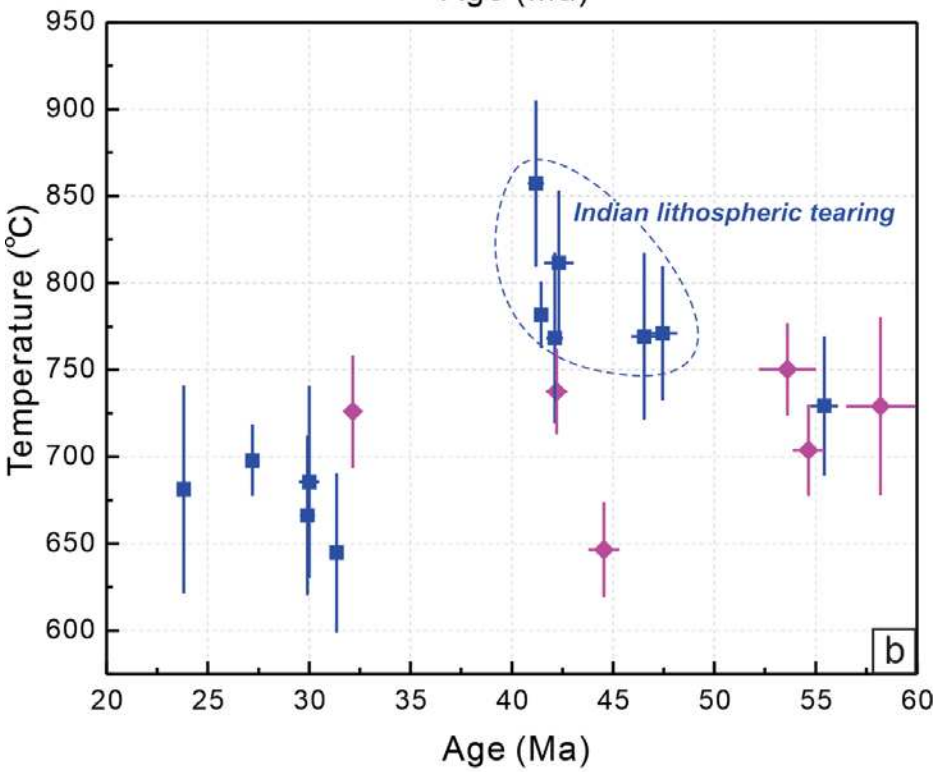
Indian lithospheric tearing
Temperature (°C)
Age (Ma)
b

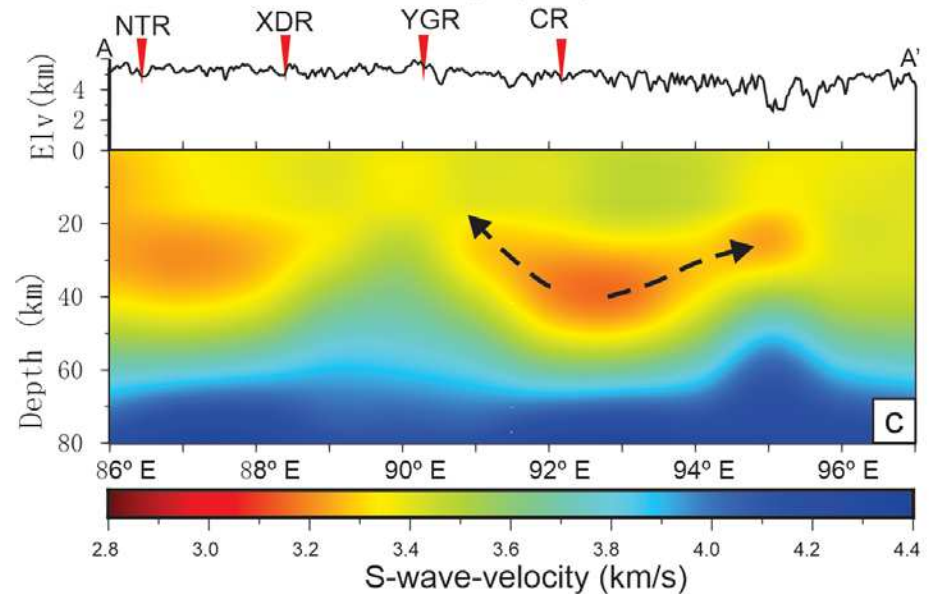
NTR
XDR
YGR
CR
A
A'
Elv (km)
Depth (km)
86° E
88° E
90° E
92° E
94° E
96° E
S-wave-velocity (km/s)
c

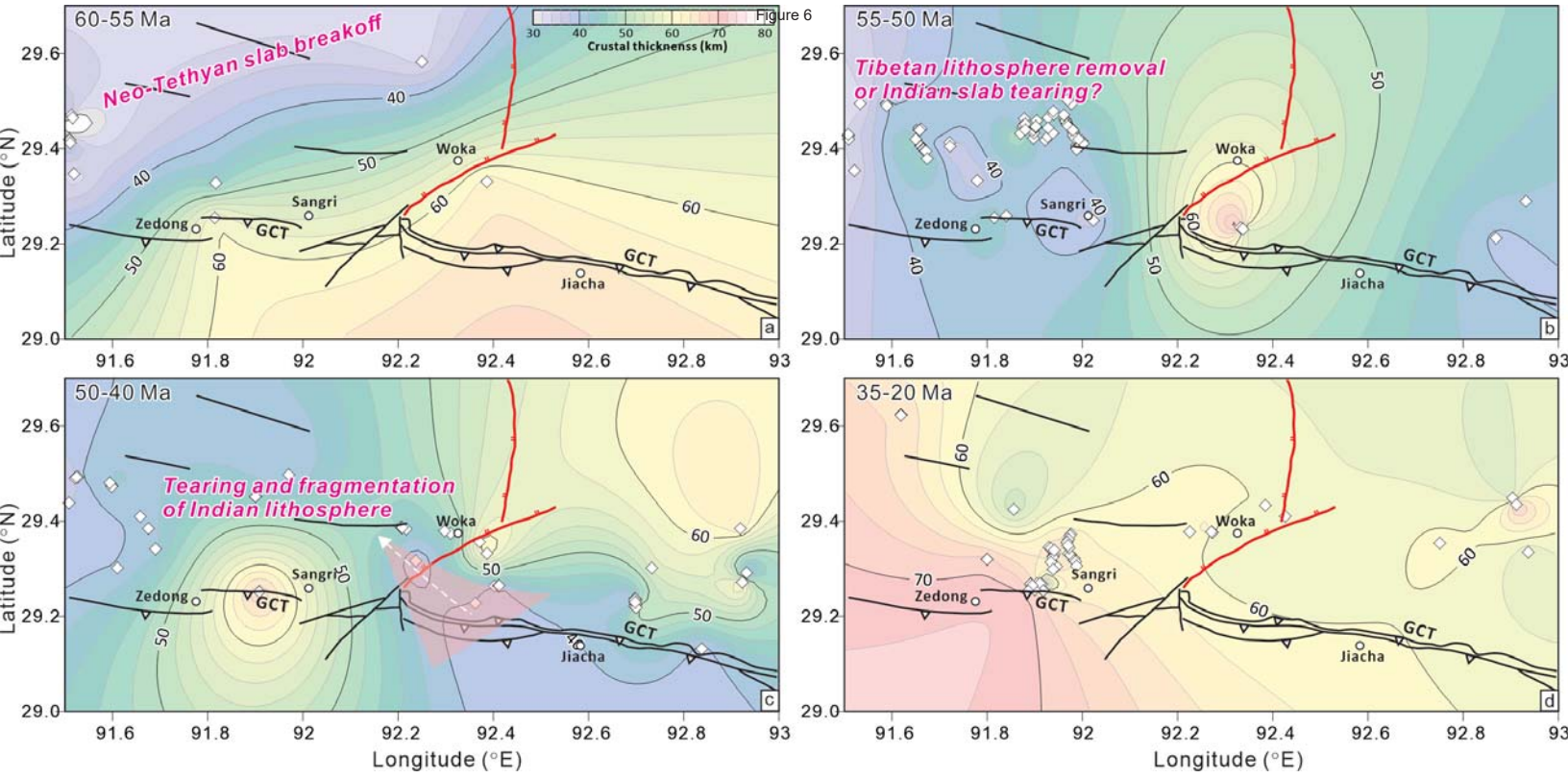
60-55 Ma
Neo-Tethyan slab breakoff
Crustal thickness (km)
30 40 50 60 70 80
Woka
Sangri
Zedong
GCT
Jiacha
a
55-50 Ma
Tibetan lithosphere removal
or Indian-slab tearing?
b
50-40 Ma
Tearing and fragmentation
of Indian lithosphere
c
35-20 Ma
d
Latitude (°N)
Longitude (°E)
29.0
29.2
29.4
29.6
91.6
91.8
92
92.2
92.4
92.6
92.8
93

Figure 6

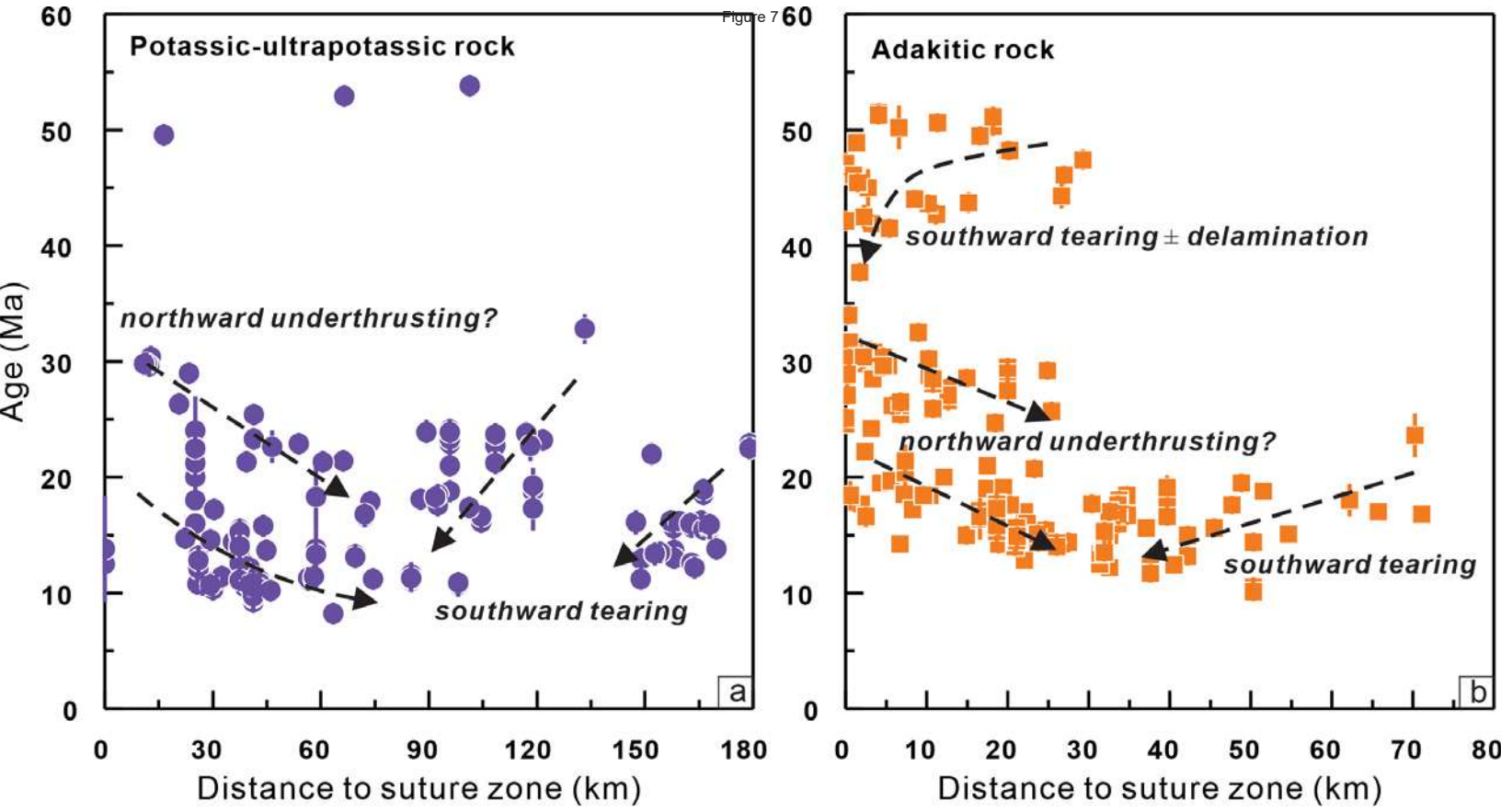
Potassic-ultrapotassic rock
northward underthrusting?
southward tearing
a
Age (Ma)
Distance to suture zone (km)
Adakitic rock
southward tearing ± delamination
northward underthrusting?
southward tearing
b
Distance to suture zone (km)

Figure 7

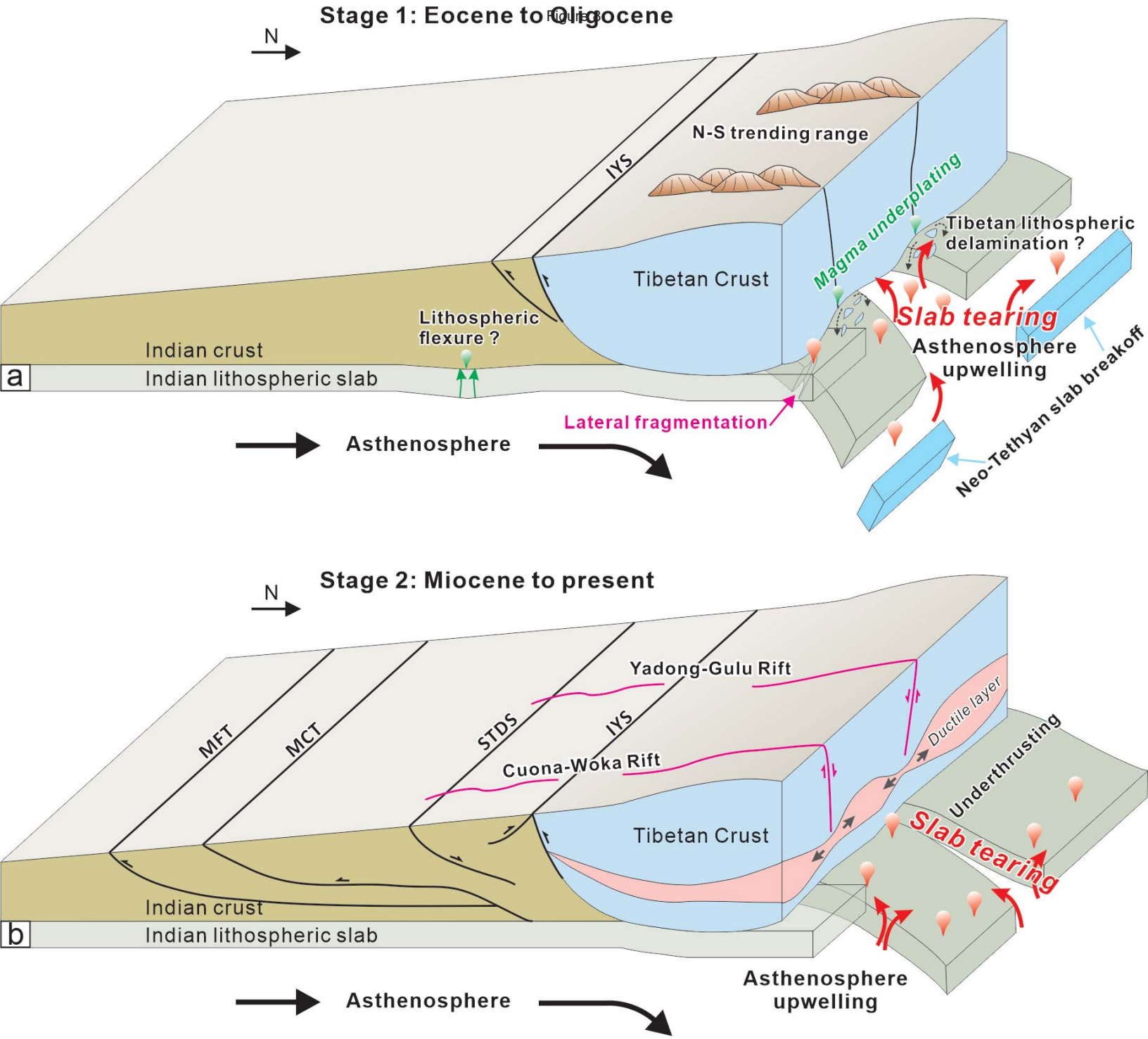
Stage 1: Eocene to Oligocene
N
N-S trending range
IYS
Tibetan Crust
Magma underplating
Tibetan lithospheric delamination ?
Slab tearing
Asthenosphere upwelling
Neo-Tethyan slab breakoff
Lithospheric flexure ?
Indian crust
Indian lithospheric slab
a
Lateral fragmentation
Asthenosphere
Stage 2: Miocene to present
N
MFT
MCT
STDS
IYS
Yadong-Gulu Rift
Cuona-Woka Rift
Ductile layer
Underthrusting
Tibetan Crust
Slab tearing
Indian crust
Indian lithospheric slab
b
Asthenosphere upwelling
Asthenosphere